

UC San Diego

UC San Diego Previously Published Works

Title

Elucidating the Detectivity Limits in Shortwave Infrared Organic Photodiodes

Permalink

<https://escholarship.org/uc/item/9vp584zh>

Journal

Advanced Functional Materials, 28(18)

ISSN

1616-301X

Authors

Wu, Zhenghui
Yao, Weichuan
London, Alexander E
et al.

Publication Date

2018-05-01

DOI

10.1002/adfm.201800391

Peer reviewed

Elucidating the Detectivity Limits in Shortwave Infrared Organic Photodiodes

Zhenghui Wu, Weichuan Yao, Alexander E. London, Jason D. Azoulay, and Tse Nga Ng*

While only few organic photodiodes have photoresponse past 1 μm , novel shortwave infrared (SWIR) polymers are emerging, and a better understanding of the limiting factors in narrow bandgap devices is critically needed to predict and advance performance. Based on state-of-the-art SWIR bulk heterojunction photodiodes, this work demonstrates a model that accounts for the increasing electric-field dependence of photocurrent in narrow bandgap materials. This physical model offers an expedient method to pinpoint the origins of efficiency losses, by decoupling the exciton dissociation efficiency and charge collection efficiency in photocurrent–voltage measurements. These results from transient photoconductivity measurements indicate that the main loss is due to poor exciton dissociation, particularly significant in photodiodes with low-energy charge-transfer states. Direct measurements of the noise components are analyzed to caution against using assumptions that could lead to an overestimation of detectivity. The devices show a peak detectivity of 5×10^{10} Jones with a spectral range up to 1.55 μm . The photodiodes are demonstrated to quantify the ethanol–water content in a mixture within 1% accuracy, conveying the potential of organics to enable economical, scalable detectors for SWIR spectroscopy.

1. Introduction

The materials used for the detection of infrared radiation are dominated by inorganic crystals that require high-temperature growth of epitaxial semiconductors and complex die-transfer and bonding processes that are not scalable. Current technologies^[1] cost tens of thousands of dollars to manufacture and are not economically viable for widespread use. Alternative semiconductors are being sought for applications in the shortwave infrared (SWIR) spectral region (wavelength $\lambda = 1\text{--}3 \mu\text{m}$), including solution-processed colloidal quantum dots,^[2–4] 2D materials,^[5] and conjugated organics,^[6–10] because solution processing allows low-temperature, direct deposition on silicon readout chips that lowers costs compared to


the time-consuming, expensive, transfer-and-bond integration processes used in current technologies. Among the novel materials, organic molecules and polymers are the most synthetically tunable, and organic bulk heterojunction (BHJ) photodiodes^[11] have demonstrated detectivities greater than silicon in the visible and near-infrared spectral regions. Given that organic BHJ solar cells show external quantum efficiency,^[12] (EQE) $> 80\%$ in the visible region, there is great potential for a polymer-based BHJ to achieve high EQE in the SWIR. Owing to a paucity of SWIR-absorbing organics,^[13,14] only a few organic SWIR photodiodes have been reported that exhibit a photoresponse past 1 μm ,^[6–10] and they show low EQE $< 10\%$ for $\lambda > 1.2 \mu\text{m}$. A better understanding of the limiting factors in narrow bandgap BHJ devices is critically needed to predict and advance performance.

This paper studies a prototypical BHJ photodiode employing a conjugated donor–acceptor copolymer with peak absorption at $\lambda = 1.2 \mu\text{m}$ and extended photoresponse to 1.55 μm , based on one of the best organic photoresponsive SWIR material sets currently available. In narrow bandgap devices, the photocurrent deviates from typical models^[15–18] used to describe the BHJ photoresponse in the visible spectrum. To reconcile these discrepancies, we present an improved model to explain the electric-field dependence of the photocurrent for SWIR photodiodes. This physical model offers an expedient method to pinpoint the origins of efficiency losses, by separating the exciton dissociation and charge collection efficiencies, as we modify device parameters such as film thicknesses and BHJ composition. Our results indicate that the main loss factor is due to poor exciton dissociation efficiency, particularly common in SWIR BHJ photodiodes with low-energy charge-transfer (CT) states. We examine the feasibility and challenges of using bandtail photoresponse to expand the spectral range of devices out to the limits of CT states. Through these examples we describe the physical model providing insights into device design guidelines and operating conditions necessary for improving EQE.

Since the figure of merit for a photodetector is the detectivity (D^*), or signal-to-noise ratio, we examine not only the photoresponse but also the origin of noise in the SWIR photodiodes. Our direct measurements of the noise power spectrum reveals that the thermally generated dark current becomes significant at narrow bandgaps. The importance of measuring and

Dr. Z. Wu, W. Yao, Prof. T. N. Ng
Department of Electrical and Computer Engineering
University of California San Diego
9500 Gilman Drive, La Jolla, CA 92093-0407, USA
E-mail: tnn046@ucsd.edu

A. E. London, Prof. J. D. Azoulay
School of Polymers and High Performance Materials
The University of Southern Mississippi
118 College Drive #5050, Hattiesburg, MS 39406, USA

 The ORCID identification number(s) for the author(s) of this article can be found under <https://doi.org/10.1002/adfm.201800391>.

DOI: 10.1002/adfm.201800391

understanding the origins^[19] of the noise current is emphasized as we clarify that calculations of D^* from a shot noise assumption may not be appropriate and can lead to overestimation by an order of magnitude. The measured results that properly include the thermal noise component show a peak detectivity of 5×10^{10} Jones. Following discussions of the design rules for maximizing D^* , we demonstrate an application of our organic BHJ photodiodes for spectroscopic analysis, which encompasses two fiber-optic windows (980 and 1310 nm) and successfully identifies alcohol content with 1% accuracy. This demonstration conveys the potential of organics to enable economical, large-area spectroscopic detectors in the SWIR spectral regions.

2. Device Structure and Performance Metric Definitions

The BHJ in this work consists of an interpenetrating network of a polymeric donor and a fullerene acceptor. The donor-acceptor copolymer (CPDT-TQ)^[9] is comprised of alternating electron-rich bridgehead olefin-substituted cyclopentadithiophene (CPDT) and electron-poor thiophene flanked [1,2,5] thiadiazolo[3,4-g]quinoxaline (TQ) building blocks, and the molecular acceptor is [6,6]-phenyl-C₇₁-butyric acid methyl ester (PC₇₁BM). Figure 1 illustrates the materials and device structures, along with the energy levels of the highest occupied molecular orbital (HOMO) and the lowest unoccupied molecular orbital (LUMO) for each material in the photodiode. Interfacial layers are incorporated to adjust electrode work functions, using zinc oxide with polyethylenimine (PEIE)^[20,21] for the cathode and molybdenum oxide (MoO₃)^[22] for the anode. As a side note, the molybdenum oxide interface is shown^[22] to aid in hole extraction but does not serve as an electron-blocking layer in organic BHJ cells. The EQE of the photodiodes with different BHJ thicknesses are shown in Figure 1c, which demonstrates

an EQE up to 10% at peak absorption at zero applied bias, with a spectral range extending to $\lambda = 1.55 \mu\text{m}$. While these devices and their performance represent the state-of-the-art level for today's organic SWIR photodiodes, we need to explain the low EQE, and in the following we determine the limiting factors and analyze the device physics for SWIR BHJ photodiodes.

For device analysis, the performance metrics are defined as follows:

- External Quantum Efficiency:** the product of the efficiencies of photon absorption, exciton dissociation, and charge collection, $\text{EQE} = \eta_{\text{absorb}} \eta_{\text{dissociate}} \eta_{\text{collect}}$.
- Internal Quantum Efficiency (IQE):** the product of exciton dissociation and charge collection, $\text{IQE} = \eta_{\text{dissociate}} \eta_{\text{collect}}$ where absorption efficiency is not counted ($\eta_{\text{absorb}} = 1$).
- Detectivity (D^*):** a signal-to-noise ratio of EQE to dark current noise. Specifically, it is defined as $D^* = (A\Delta f)^{0.5} R/i_n$, where R is the responsivity related to $\text{EQE} = R(hc/\lambda q) = (J_{\text{ph}}/P_{\text{illum}})(hc/\lambda q)$, A is the effective photodetector area, Δf is the detection bandwidth, i_n is the noise current measured in the dark, h is Planck's constant, c is the speed of light, λ is the wavelength of the incident light, q is the electron charge, J_{ph} is the photocurrent density, and P_{illum} is the intensity of the incident light.

3. Results and Discussions

3.1. An Improved Model to Describe Photocurrent in Organic SWIR Photodiodes

Figure 2a shows the typical photocurrent density–voltage characteristics of an organic SWIR photodiode. The photocurrent density $J_{\text{ph}}(V) = J_{\text{L}}(V) - J_{\text{D}}(V)$ is the difference between the current density under illumination J_{L} and the dark current density J_{D} . The voltage, $V_{\text{built-in}}$, is the built-in potential at which the photocurrent density is canceled, namely when $J_{\text{L}} = J_{\text{D}}$. In Figure 2b, the J_{ph} data are plotted against the effective electric field $E_{\text{eff}} = V_{\text{eff}}/d$, where the effective voltage is $V_{\text{eff}} = V_{\text{built-in}} - V$, with V being the applied bias and d the BHJ thickness. Prior work on BHJ describes the electric-field dependence of photocurrent density using the Hecht equation^[23,24]

$$J_{\text{ph}} = J_{\text{sat}} \cdot \frac{2\mu\tau V_{\text{eff}}}{d^2} \left[1 - \exp\left(-\frac{d^2}{2\mu\tau V_{\text{eff}}}\right) \right] \quad (1)$$

$$= J_{\text{sat}} \cdot \eta_{\text{collect}}(E_{\text{eff}})$$

where J_{sat} is the saturated photocurrent density dependent on the amount of absorbed light, and $\mu\tau$ is the mobility–lifetime product that characterizes the capture cross section and density of recombination centers. The μ and τ are not independent variables; the value of $\mu\tau$ reflects the extent of bimolecular recombination^[25] or recombination via

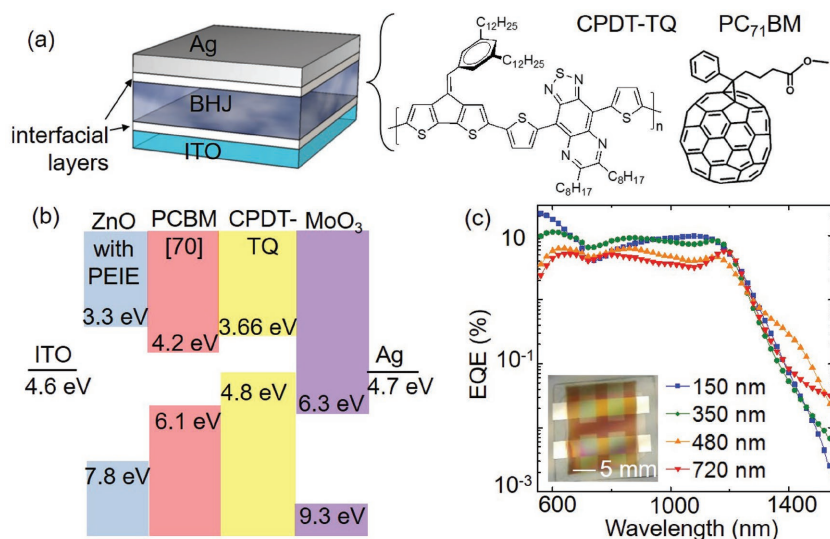


Figure 1. a) Device and materials structures. b) The HOMO/LUMO energy levels for each material in the photodiode. c) External quantum efficiencies of photodiodes with different BHJ thicknesses. The inset is a photograph of four SWIR CPDT-TQ:PC₇₁BM photodiodes, each with an active area of 9 mm².

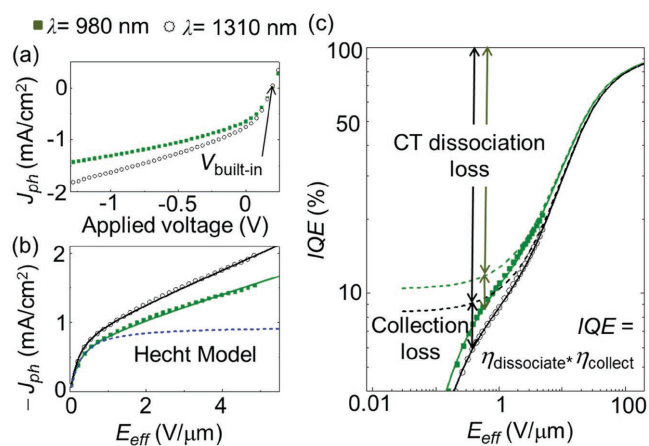


Figure 2. a) Photocurrent density versus bias voltage under laser diode illumination, at 10.5 mW cm^{-2} for $\lambda = 980 \text{ nm}$ and at 250 mW cm^{-2} for $\lambda = 1310 \text{ nm}$. This photodiode has a BHJ thickness of 350 nm . b) Photocurrent density versus the effective electric field, with fits according to the Hecht model (blue dashed line) or to the improved model of Equation (3) (solid lines). c) Internal quantum efficiency versus effective electric field. The markers represent experimental data. The dashed lines are calculated according to the Braun/Mihailetchi CT dissociation model. The solid lines are fit lines based on Equation (3).

localized states.^[23] For example, in a device affected by bimolecular recombination due to an increase in carrier density under intense illumination, the $\mu\tau$ value decreases, reflecting a $J_{\text{ph}}-V$ characteristics with low fill factor.^[18] The phenomenological Hecht equation often fits very well to the $J_{\text{ph}}-V$ characteristics of typical organic BHJ solar cells made from large bandgap polymers, for which the main limitation is recombination in the charge collection process.^[26]

However, in the SWIR photodiodes with narrow bandgap, the electric-field dependence of photocurrent is not fully accounted for by the Hecht model. The dashed line in Figure 2b is a fitted curve based on Equation (1), and the poor fit indicates that the Hecht model is insufficient to describe the data across the range of electric fields. The Hecht equation attributes the electric-field dependence of photocurrent solely to recombination losses during charge collection, as the Hecht model assumes a “constant” exciton dissociation efficiency over all electric fields. It overlooks that exciton dissociation processes can vary with the electric field, depending on the BHJ energy-level alignment. In BHJs with a large offset between donor-acceptor LUMO levels, the exciton dissociation approaches 100%, while in BHJs with small donor-acceptor LUMO offset, the exciton dissociation efficiency is low and can be increased by applying an electric field.^[27–29] The latter case requires modifications to the Hecht model.

The electric-field dependence of exciton dissociation must be considered to describe the SWIR devices in this work. Braun^[15] and Mihailetchi et al.^[16,17,30] modeled the rates of exciton dissociation k_{D} and recombination k_{R} by invoking that excitons at CT states^[31,32] have a finite lifetime and either dissociate into free carriers at rate k_{D} or decay back to ground states at rate k_{R} . The dissociation rate k_{D} is electric-field dependent, while k_{R} is independent of electric field. The dissociation efficiency is expressed by

$$\eta_{\text{dissociate}}(E_{\text{eff}}) = k_{\text{D}}(E_{\text{eff}}) / [k_{\text{D}}(E_{\text{eff}}) + k_{\text{R}}].$$

The rate k_{D} is dependent on $k_{\text{D}}(E_{\text{eff}}) = \frac{3q\langle\mu\rangle}{4\pi\epsilon_0\epsilon_r a^3} \exp(-\frac{E_{\text{B}}}{kT}) [1 + b + \frac{b^2}{3} + \frac{b^3}{18} + \dots]$, where $E_{\text{B}} = \frac{q^2}{4\pi\epsilon_0\epsilon_r a}$ is the binding energy of CT exciton; $b = \frac{q^3 E_{\text{eff}}}{8\pi\epsilon_0\epsilon_r k^2 T^2}$; $\langle\mu\rangle$ is the local carrier mobility,^[33] a is the initial separation distance between the electron and the hole in a CT exciton; ϵ_0 is the vacuum permittivity; ϵ_r is the dielectric constant of BHJ; k is the Boltzmann constant; and T is the temperature, and for this paper $T = 295 \text{ K}$. The physical parameters $\epsilon_r = 3.4$ and $a = 1.3 \text{ nm}$ are fixed in this work based on materials properties. Due to the Gaussian distribution of states in organics, the dissociation efficiency $\eta_{\text{dissociate}}(E_{\text{eff}})$ is integrated over the electron–hole pair separation distance x , to be found as

$$\eta_{\text{dissociate}}(E_{\text{eff}}) = \frac{4}{\sqrt{\pi}a^3} \int_0^{\infty} \eta_{\text{dissociate}}(x, E_{\text{eff}}) F(x) dx \quad (2)$$

where $F(x) = x^2 \cdot \exp(-x^2/a^2)$ is the state distribution function.

The functional form of the dissociation probability $\eta_{\text{dissociate}}(E_{\text{eff}})$ is an “S-shaped” curve increasing with the electric field, visualized by the dashed lines in Figure 2c. To aid readers in exploring this dissociation model by Braun and Mihailetchi *et al.*, we include computational analyses in Figure S1 (Supporting Information) on how the physical parameters ϵ_r , a , $\langle\mu\rangle$, and k_{R} affect the dissociation probability of CT states. In comparison to typical organic solar cells, the dissociation probability in SWIR devices is worse due to the lower built-in electric field from the reduced CT-state bandgap and higher thermal decay of CT excitons.^[12,34] Note the experimental data deviate from the above dissociation model especially at low fields in Figure 2c, because Equation (2) is not designed to include the effects of other processes, such as charge collection on the photocurrent.

We account for the electric-field dependence of both exciton dissociation and charge collection processes in order to arrive at a general phenomenological expression for the photocurrent density. We combine Equations (1) and (2) and obtain the following formula to fit to data and study the dissociation and collection efficiencies in our SWIR photodiodes

$$J_{\text{ph}} = J_{\text{sat}} \cdot \frac{2\mu\tau E_{\text{eff}}}{d} \left[1 - \exp\left(-\frac{d}{2\mu\tau E_{\text{eff}}}\right) \right] \cdot \eta_{\text{dissociate}}(E_{\text{eff}}) \quad (3) \\ = J_{\text{sat}} \cdot \eta_{\text{collect}}(E_{\text{eff}}) \cdot \eta_{\text{dissociate}}(E_{\text{eff}})$$

We determined the values in **Table 1** by fitting Equation (3) to the photocurrent densities in Figure 2b.

The fitting parameters $\langle\mu\rangle$ and k_{R} relate to dissociation; $\mu\tau/d^2$ describes charge transport; and J_{sat} depends on incident light power. The photocurrent density is converted to IQE through dividing $J_{\text{ph}}(E_{\text{eff}})$ by J_{sat} . As seen in Figure 2b,c, Equation (3) fits very well to the experimental data across all electric fields, because our model eliminates the assumptions of either constant dissociation or collection in the individual Hecht or Braun/Mihailetchi model, respectively.

The improved model as denoted by Equation (3) offers a straightforward method to separate the efficiencies of exciton

Table 1. Fit values to Equation (3) for the device in Figure 2 illuminated by 980 or 1310 nm light, under different incident power. The physical parameters $\epsilon_r = 3.4$ and $a = 1.3$ nm are fixed in this work based on materials properties.

illumination, λ [nm]	980	1310
Light power [mW cm ⁻²]	10.5	250
$\langle\mu\rangle$ [10 ⁻³ cm ² V ⁻¹ s ⁻¹]	1.0 ± 0.1	1.0 ± 0.1
$\mu\tau/d^2$ [V ⁻¹]	4.0 ± 0.3	4.0 ± 0.3
J_{sat} [mA cm ⁻²]	7.4 ± 0.2	10.8 ± 0.2
k_R [10 ⁷ s ⁻¹]	1.4 ± 0.1	1.9 ± 0.1
The following values are reported for an applied bias $V = 0$ V, where $E_{\text{eff}} = 0.6$ V μm^{-1} :		
$\eta_{\text{dissociate}}$ [%]	12 ± 0.2	9.5 ± 0.2
η_{collect} [%]	75 ± 2	74 ± 2
IQE [%]	9.0 ± 0.3	7.0 ± 0.3

dissociation and charge collection processes, and subsequently identify the limiting mechanism. The fit values to Equation (3) are used to calculate IQE over a large range of electric fields. Specifically in Figure 2c, the dashed line represents the Braun/Mihaleitchi model that assumes $\eta_{\text{collect}}(E_{\text{eff}}) = 100\%$, such that IQE depends on $\eta_{\text{dissociate}}(E_{\text{eff}})$ only. At electric fields below 2 V μm^{-1} , the measured data deviate from the dashed line, and the difference quantifies the drop in charge collection efficiency from 100%. At electric fields above 2 V μm^{-1} , the measured data follow the dashed line quite closely, indicating that the electric field is sufficiently high to reach 100% charge collection, and consequently the IQE drop is attributed to inefficient exciton dissociation. For example, based on fit values to Equation (3) and the graphical analysis in Figure 2c, the dissociation efficiency is at 12% while collection efficiency is 75% at zero applied bias (where $E_{\text{eff}} = 0.6$ V μm^{-1}) under an illumination

wavelength of 980 nm. Thus, the low IQE in SWIR photodiodes is mainly due to poor dissociation efficiency, and electric-field dependence of exciton dissociation plays an important role in the narrow bandgap materials.

3.1.1. Electric-Field Dependence of Exciton Dissociation Probed by Measurements of Transient Photoconductivity versus Applied Voltage

Since our fit results indicate a field-dependent charge generation process, we test this interpretation with independent measurements of transient photoconductivity^[26,35] (Figure 3) to check the dissociation loss versus the transport loss. As explained in detail in ref. [35], transient photoconductivity differentiates the two loss mechanisms, by measuring the photocurrent from the mobile carriers at short times to extract the initial charge density before significant bimolecular recombination or charge collection occurs. If the exciton dissociation process is not efficient, an externally applied voltage provides an additional electric field to separate the electron-hole pairs, and hence the initial charge density will increase with an increasing reverse bias. On the other hand, if the dissociation process is efficient, all the electron-hole pairs are already separated into free carriers; an external bias will have minimal effect on the initial charge density. Then the initial charge density will be relatively constant across the range of applied voltages, and this scenario has been observed in BHJ solar cells.^[34,35] Here we measure the transient photoconductivity of our SWIR CPDT-TQ:PC₇₁BM photodiodes and compare it to a P3HT:PC₇₁BM device with a CT-state bandgap of 1.0 eV, which is 0.4 eV larger than the SWIR devices here.

The transient photocurrent density is expressed as $J_{\text{ph}}(V, t_{0+}) = q\langle\mu\rangle N(V, t_{0+})V_{\text{eff}}/d$, where t_{0+} denotes the time just after the illumination pulse, $\langle\mu\rangle = d^2/(t_{\text{tr}}V_{\text{eff}})$ is the average mobility estimated from the carrier transit time t_{tr} (namely,

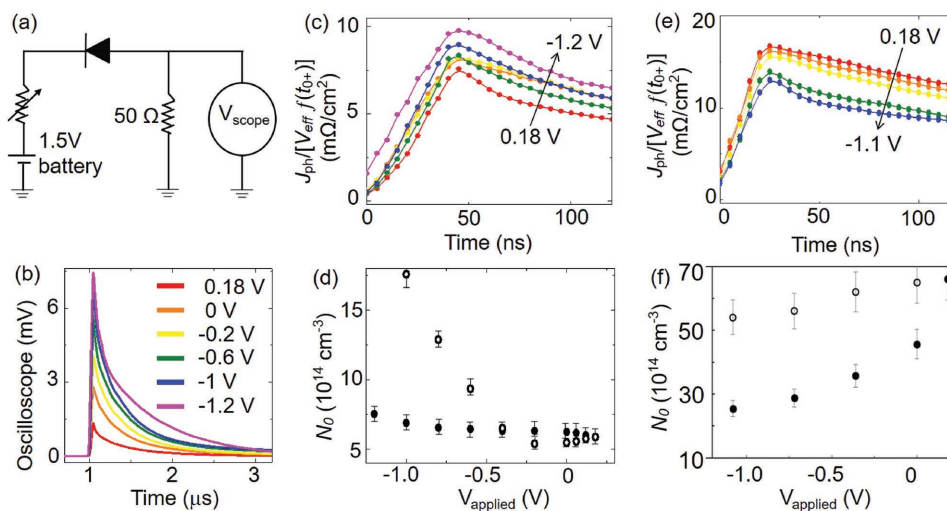


Figure 3. a) Schematics of the transient photoconductivity measurement. b) Transient voltage under different applied bias on the SWIR photodiode. c,d) Transient photoconductivity taken on the SWIR CPDT-TQ:PC₇₁BM device and e,f) on the P3HT:PC₇₁BM device. c,e) Transient photoconductivity and d,f) carrier density after the excitation pulse at different applied voltages. The direction of the arrows in panels (c) and (e) indicates increasing reverse bias. In panels (d) and (f), the solid markers are data extracted based on the assumption of a constant μ , while the open markers account for $\mu = \mu_0 \sqrt{E_{\text{eff}}}$.

the time when the transient photocurrent decays to $1/e$ of the peak value), and $N(V, t_{0+})$ is the photogenerated charge density soon after the illumination pulse. The mobile charge density is $N(V, t_{0+}) = N_0(V)f(t_{0+}) = N_0(V)\left[1 - \frac{\langle\mu\rangle t_{0+} V_{\text{eff}}}{d^2}\right]$, where the function $f(t_{0+})$ accounts for the percentage of charge collected within the rise time of the measurement circuit; the rise time equals to the product of resistance (R) and capacitance (C) of the circuit.^[35] Hence, the initial charge density $N_0(V)$ at an applied voltage is given by

$$\frac{J_{\text{ph}}(V, t_{0+})}{V_{\text{eff}}} \frac{1}{\left[1 - \frac{\langle\mu\rangle t_{0+} V_{\text{eff}}}{d^2}\right]} = N_0(V) q \langle\mu\rangle / d \quad (4)$$

All the parameters used in the following $N_0(V)$ calculations are directly measured quantities or material constants. The initial charge density for the SWIR device and the P3HT:PC₇₁BM device in Figure 3 is estimated at t_{0+} of 60 and 40 ns, respectively, immediately following the transient peak signal.

Figure 3b shows a typical series of the transient voltage traces $V_{\text{oscilloscope}}$ under various biases, and the signals are converted to J_{ph} by $J_{\text{ph}} = V_{\text{oscilloscope}} / (R_{\text{load}} \cdot \text{area})$, where R_{load} is a resistor of 50 Ω and the photodiode area is 9 mm². In Figure 3c, we compare the transient photoconductivity $J_{\text{ph}}/[V_{\text{eff}} f(t_{0+})]$ of the SWIR device at 60 ns after the illumination pulse. With higher reverse bias, the transient photoconductivity value increases. The extracted initial carrier density $N_0(V)$ increases with the applied bias in Figure 3d. This trend is indicative of an electric-field-dependent dissociation process in which more free carriers are generated with the aid of an external voltage applied to the SWIR photodiode.

In contrast, the measurements on a P3HT:PC₇₁BM device show a very different transient photoconductivity response in Figure 3e,f, where the $J_{\text{ph}}/[V_{\text{eff}} f(t_{0+})]$ and $N_0(V)$ values do not increase upon applying external bias. One caution regarding the analysis of the poly-3-hexylthiophene (P3HT) blend device involves accounting for the electric-field dependence of mobility. In Equation (4), the mobility μ is not constant over the range of electric fields. For organics it is well known that mobility increases with the electric field^[30] by $\langle\mu\rangle = \mu_0 \sqrt{E}$. After the adjustment, $N_0(V)$ is shown by the open markers in Figure 3d,f. For P3HT:PC₇₁BM, the initial charge density is relatively constant and maximized regardless of the external fields, while for the SWIR blend, the amount of photogenerated charge can be further increased with higher field, indicating field-assisted dissociation. The transient photoconductivity results confirm that exciton dissociation is a limiting factor for the SWIR photodiodes based on narrow bandgap polymers.

Besides the processes of exciton dissociation and free carrier recombination, there are two other conditions that may potentially contribute to the electric-field dependence of photocurrent: (1) a high density of deep trap states and (2) a high leakage current. For condition 1, if many mobile carriers are captured by deep traps and detrapping is relatively slow, the device may exhibit severe time-dependent J - V hysteresis due to photoconductive gain, and Equation (3) does not apply. A high density of deep traps and space charges would be revealed in the low-frequency region of electrochemical impedance spectroscopy (EIS) measurements.^[36] The J - V and EIS data of our SWIR

devices do not show hysteresis or a significant amount of deep traps (Figure S2, Supporting Information). For condition 2, if high leakage current is an issue, the shunt resistance would be similar to the series resistance in the EIS data, which is not the case for our devices. Both of the above conditions are not observed in our SWIR devices and do not contribute to the electric-field dependence of photocurrent.

3.1.2. Delineating $\eta_{\text{dissociate}}$, η_{collect} under Different Spectral Regions

Fitting $J_{\text{ph}}-V$ characteristics to Equation (3) allows us to isolate the physical parameters that are affected under different stimuli or by device designs (details of BHJ composition in Figure S3 in the Supporting Information). For instance, when the incident excitation wavelength is changed in Figure 2, we observe that the device under 1310 nm light shows greater electric-field dependence than the same device under 980 nm light. After accounting for the differences in incident power through normalization by J_{sat} , the IQE is found to be lower under the longer wavelength light in the BHJ absorption bandtail. To interpret this spectral effect, we find via fitting data to Equation (3) that the transport parameters $\langle\mu\rangle$ and $\mu\tau/d^2$ are not influenced by incident wavelength, but the parameter k_{R} is reduced under 980 nm light (Table 1). The decrease in recombination rate k_{R} with shorter wavelength light is due to the higher energy excitons, in which the excess energy released in the charge-transfer process^[37] improves dissociation probability.

3.1.3. Delineating η_{absorb} , $\eta_{\text{dissociate}}$, and η_{collect} in Devices with Different BHJ Thicknesses

Since high electric-field dependence is observed in the photocurrent measurements, we proceeded to vary the BHJ film thickness, which in effect changes the built-in electric field in the photodiodes. The BHJ thickness affects both the photocurrent and dark current noise. Our discussion in the following section focuses on the photoresponse, and Section 3.2 will explain noise and the resulting detectivity.

Figure 4a displays the $J_{\text{ph}}-V$ characteristics for a set of SWIR photodiodes with BHJ thickness d ranging from 150 to 720 nm. Under similar incident power from a laser of $\lambda = 980$ nm, the photocurrent density decreases with increasing film thickness. The x -axis in Figure 4a is converted from the applied voltage to the effective electric field in Figure 4b; after the x -axis conversion, the trends in Figure 4a,b appear different because of the normalization over thickness. To understand how thickness affects the efficiencies of dissociation and collection processes, the photocurrent density is converted to IQE versus the effective electric field, and the data are fitted to Equation (3) with the resulting values included in Table ST1 (Supporting Information). Figure 4c shows enhanced IQE by using thinner BHJ films. If the devices are operated specifically at zero applied bias where $E_{\text{eff}} = V_{\text{built-in}}/d$, both $\eta_{\text{dissociate}}(E_{\text{eff}})$ and $\eta_{\text{collect}}(E_{\text{eff}})$ are increased in a thinner BHJ due to the higher internal electric field.

The BHJ thickness affects the absorption efficiency in an opposite trend to the dissociation or the collection process, as light absorption increases with thicker BHJ film. We

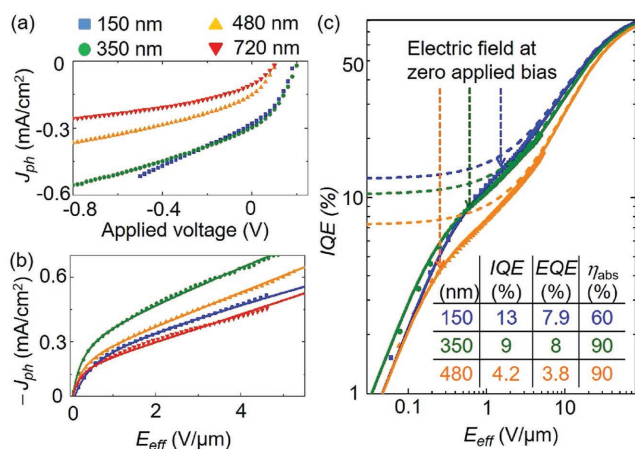


Figure 4. a) Photocurrent density versus applied voltage, b) photocurrent versus effective electric field, and c) internal quantum efficiency versus the effective electric field for devices with different BHJ thicknesses. The solid lines are fits to Equation (3). The dashed lines are calculated from Equation (2) which assumes $\eta_{dissociate}(E) = 100\%$. The dashed arrows indicate the magnitudes of internal E_{eff} at zero applied bias; the IQE, EQE, and extracted η_{absorb} efficiency at zero applied bias are listed in the inset. For clarity, the device with 720 nm BHJ was omitted in panel (c) but its fit values are reported in Table S1 (Supporting Information).

examine the thickness dependence of η_{absorb} in two ways: (1) by extracting it through $\eta_{absorb} = EQE/IQE$ using the measured EQE and IQE in Figure 4c; and (2) by measuring the photodiode reflectance spectra, shown in Figure S4 (Supporting Information). The independent measurements confirm the reliability of the results for η_{absorb} . Due to the interference effect of light through multiple subwavelength thin films and the high absorption coefficient of the organic BHJ, the reflectance spectra of our devices show $\eta_{absorb} = 60\%$ at a BHJ thickness of 150 nm and saturates to $\eta_{absorb} = 90\%$ at a thickness of 350 nm, under an illumination wavelength of 980 nm. Therefore, despite the thin absorption layer in our devices, η_{absorb} is high and not the main bottleneck for wavelengths above the polymer optical bandgap. Peak absorption efficiencies as high as 80% have been previously reported in organic solar cell containing only 80 nm BHJ.^[38–40] Accounting for all the contributions (η_{absorb} , $\eta_{dissociate}$, $\eta_{collect}$) to photocurrent, the EQE values are similar between the BHJ thickness of 150 and 350 nm as shown in Figures 1c and 4c. For the 350 nm photodiode, the lower IQE is compensated by an increased η_{absorb} in comparison to the 150 nm device.

3.1.4. Comparison of EQE in Spectral Regions Above or Below the Donor Optical Bandgap

Due to the wide distribution of bandtail states in organic semiconductors, there is measurable photoresponse below the donor optical bandgap, in the bandtail spectral range of $\lambda = 1200\text{--}1600$ nm (Figure 1). The bandtail photoresponse offers an alternative approach to extend the device's spectral range beyond the donor bandgap. Theoretically, the minimum energy, or the longest wavelength, that can be absorbed by a BHJ photodiode is defined by the energy gap of the CT state. For organic

BHJ, increases in trap states have been observed over operation time,^[41] and subsequently the spectral response at the bandtail is slightly increased due to the trap states. However, the bandtail approach so far is restricted to low efficiencies, because the bandtail states often act as recombination centers for free carriers. As discussed earlier in Figure 2, $\eta_{dissociate}$ is reduced for bandtail excitons due to higher recombination rate. In terms of η_{absorb} , even with a thick film of 480 nm, the sum of the absorption from the BHJ and electrodes is less than 50% in the bandtail region (Figure S4, Supporting Information). Increasing BHJ film thickness to increase η_{absorb} will adversely affect $\eta_{dissociate}$ and $\eta_{collect}$, both of which rapidly drop with thickness (Figure 4). To leverage the bandtail response, other researchers have employed an optical cavity^[10,42] to increase absorption without raising the BHJ thickness. Using this approach, the reported EQE is enhanced to 20% at $\lambda = 900$ nm but beyond that wavelength the EQE is limited to $<1\%$. The bandtail photoresponse offers an extension to the photodiode spectral range but currently operating in the bandtail is not efficient. For devices without optical structures such as microcavity and plasmonic structures, it is preferable to tune the peak absorption of the donor polymer and reduce bandtail states, because a reduction in bandtail states will mitigate thermal decay and improve the main bottleneck in dissociation efficiency. A recent study^[43] shows a promising path to enhance exciton lifetime by promoting aggregate delocalization in SWIR materials, and such morphological control may broaden the spectral response in future work.

3.2. Identifying Dominant Noise Source and Avoiding Overestimation of Detectivity

For photodiodes acting as a detector, a key figure of merit is the detectivity D^* (defined in Section 2), which, in addition to photoresponse, requires accurate assessment of the dark current noise i_n . Dark current measured with a power spectrum analyzer gives the noise spectral density $i_n (\Delta f)^{-0.5}$ in Figure 5a that accounts for all the noise components^[19]—shot noise, thermal noise, and $1/f$ noise. Here, the $1/f$ noise is negligible at frequencies beyond 100 Hz. Individual white noise components can be estimated from equations in Figure 5; the shot noise is calculated from the dark current versus voltage (J_D - V) characteristics (Figure 5b), and the thermal noise is computed with the shunt resistance R_{SH} obtained through impedance spectroscopy (Figure 5c). The shot noise near zero external bias is $\approx 10^{-14}$ A Hz^{-0.5}, an order of magnitude lower than the thermal noise. In comparison to photodiodes for visible wavelengths, thermal generation becomes significant in narrow bandgap SWIR materials, and thermal noise overtakes shot noise as the dominant noise source. This analysis emphasizes the importance of direct noise measurement to account for all the noise components; otherwise, using a shot noise assumption alone, the detectivity will be overestimated by an order of magnitude.

As thermal noise is the major noise source, improving shunt resistance will be key to mitigate noise. Increasing the thickness of BHJ slightly raises shunt resistance, from $R_{SH} = 32$ k Ω for a 150 nm film to $R_{SH} = 48$ k Ω for a 480 nm film. A further thickness increase did not improve R_{SH} , because there is a

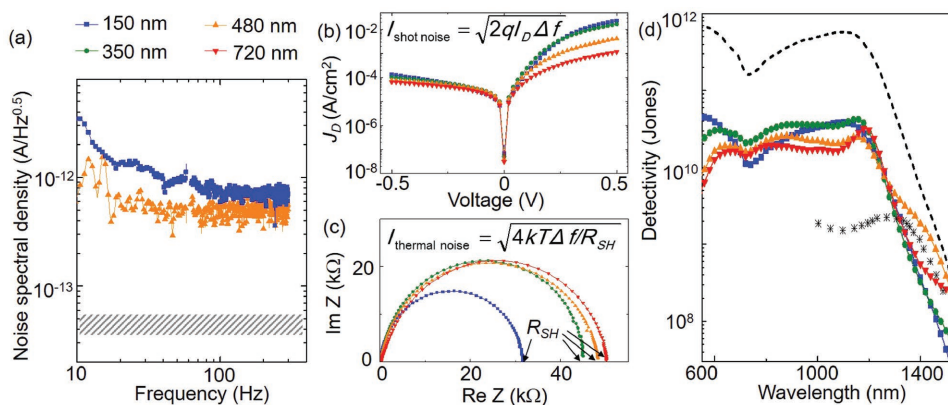


Figure 5. a) Noise spectral density of photodiodes with different BHJ thicknesses at zero external bias. For clarity, only two thicknesses are shown. The shaded area indicates the shot noise level calculated from the dark current measured at -0.1 mV, for BHJ thickness between 150 and 720 nm. b) Dark current versus applied bias. c) Shunt resistance estimated from impedance spectroscopy at zero external bias. d) Detectivity calculated according to the actual measured noise (colored traces). The dashed line represent an overestimated detectivity calculated using only shot noise. The star markers represent the detectivity of a previously reported SWIR photodiode^[44] based on a blend of organics and quantum dots.

trade-off between a long carrier collection path, countered by an increased volume for thermal generation of carriers. The detectivities of photodiodes with different BHJ thicknesses are similar (Figure 5d). Research on electrode interfacial layers is ongoing to improve shunt resistance. For our SWIR photodiodes under reverse bias, there is a sharp rise in noise that is only partially compensated by a minor EQE improvement. At an applied bias of -0.2 V, the noise current density is at least three times that at zero bias, while the photocurrent only increases by about 30% (similar results found in ref. [45]). The overall detectivity is worse under reverse bias than at zero external bias. Thus, to maximize detectivity in the above devices, it is preferable to operate at zero external bias and use BHJ film thickness of ≤ 350 nm. Our set of SWIR photodiodes reach a detectivity up to 5×10^{10} Jones, which is higher than that of devices using a blend^[44] of organics and quantum dots. The main reason for the increased performance is the lower leakage current and noise in our devices, compared to the quantum dot blends with high leakage current probably due to rough morphology.

3.3. Example of Spectroscopic Analysis via Organic SWIR Photodiodes

Since our photodiodes provide a spectral range up to 1550 nm, they allow demonstration of spectroscopic analysis at wavelengths relevant to applications such as medical oximetry,^[45–47] biological imaging with deep penetration depth,^[48] or internet-of-things applications^[49] that monitor water content in agricultural or industrial process inspections. For instance, water and alcohol are indistinguishable in the visible spectrum, but they differ in absorption for $\lambda > 1200$ nm. Figure 6 illustrates an example of determining the ethanol percentage in water. As measured with an organic SWIR photodiode, light transmission increases with ethanol content in the spectral range between 1200 and 1400 nm, whereas the transmission percentages are constant at $\lambda = 920$ and 1190 nm for all the samples. The transmission spectrum of a beer sample (brand: Modelo Especial) is also measured; due to light scattering from

CO₂ bubbles in the beer, we adjust the beer spectrum to the same baseline transmission values at $\lambda = 920$ and 1190 nm. After this baseline adjustment, the beer spectrum matches well to the spectra of a 5% ethanol–water mixture, in agreement with the manufacturer’s value. Due to a gradual shift in absorption peak with increasing ethanol content, the calibration curve in Figure 6c is obtained from the range of $\lambda = 1260$ –1340 nm, and the y -axis values are calculated from $1/n \left[\sum_{0, \lambda=1260 \text{ nm}}^n \%T(\text{sample}) - \sum_{0, \lambda=1260 \text{ nm}}^n \%T(\text{water}) \right]$, in which there were nine data points ($n = 9$) to be averaged in the chosen spectral range. In contrast to simple subtraction at a single wavelength, this integration method yields a calibration curve with higher accuracy, with an error bar of $\pm 0.5\%$ in determining the ethanol content in a sample.

4. Conclusions

Based on state-of-the-art SWIR BHJ photodiodes, this paper demonstrates a straightforward method to decouple the exciton dissociation efficiency and charge collection efficiency in photocurrent–voltage measurements. The physical model offers an accessible analytical tool to identify the limiting factors to organic SWIR photodiode performance; this new model is needed to properly account for the increasing electric-field dependence of photocurrent processes in narrow bandgap materials. Our results provide an understanding of the fundamental properties necessary to extend the utility of organics into a field now completely dominated by inorganic materials. In addition to improving the parameters ($\downarrow k_R$, $\uparrow \langle \mu \rangle$, $\uparrow \mu\tau/d^2$, $\uparrow E$), maximizing built-in electric field is essential to improve the main bottleneck in dissociation efficiency. This study shows that the dominant noise source in organic SWIR devices is thermal noise, not shot noise as is typical with photodetectors operating in the visible spectrum. To optimize detectivity in the CPDT-TQ:PCBM photodiodes, it is preferable to operate the devices at zero external bias and use BHJ film thickness of ≤ 350 nm in order to balance the requirements for IQE, η_{abs} , and thermal noise. As novel organic materials emerge, the device design rules discussed here will be

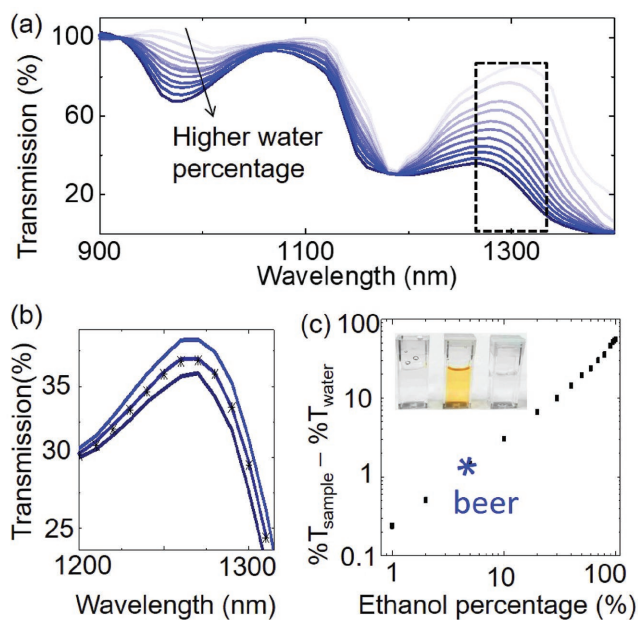


Figure 6. Demonstration of spectroscopic analysis using an organic SWIR BHJ photodiode. a) Transmission spectra of deionized water, water–ethanol mixtures, and ethanol. The water content increases from 0% to 100% by a step of 10%. b) Zoom-in view of the transmission spectra for beer (asterisk markers) and mixtures of DI water with 10%, 5%, and 1% ethanol (top blue curve: 10% ethanol; bottom black curve: 1% ethanol). c) Percentage change in transmission as a function of ethanol content in DI water. This calibration curve is based on the data from the spectral range of $\lambda = 1260\text{--}1340$ nm, indicated by the dashed box in panel (a). Inset is a photo of the water, beer, and ethanol samples (left to right).

applicable to other SWIR BHJ systems and will be useful for guiding the development of economical, scalable organic detectors for the SWIR spectrum.

5. Experimental Methods

Materials: The synthesis process and basic chemical properties of the polymer CPDT-TQ is published in ref. [9]. The fullerene derivative PC₇₁BM and regioregular P3HT were bought from Ossila Ltd. The MoO₃, Ag, and the cathode interfacial layer PEIE (35–40 wt% in water, molecular weight: 7000 g mol⁻¹) were purchased from Sigma-Aldrich. ZnO nanoparticles were synthesized from zinc acetate dihydrate and potassium hydroxide, following the procedure described by Hermann-Jens Womelsdorf.^[50] The chemicals were used as purchased without further purification.

Fabrication: The prepatterned indium tin oxide (ITO) substrates were ultrasonically cleaned in detergent, deionized (DI) water, and 2-propanol for 15 min sequentially. PEIE was diluted by 2-methoxyethanol to achieve a concentration of 0.4% by weight and mixed with ZnO nanoparticles in a ratio of 2:1 by weight. The mixture was cast onto a cleaned ITO substrate at a spin speed of 3500 rpm to form a ≈ 10 nm film, which was annealed at 120 °C for 10 min in ambient. The polymer and PC₇₁BM in 1:2 ratios were dissolved in dichlorobenzene with 3% of 1,8-diiodooctane as

additive. The solutions were stirred on a hot plate at 80 °C overnight in N₂ atmosphere. Then the solution was cooled to 45 °C and was spincoated on the PEIE/ITO substrate with different spin speeds to form BHJs of different thicknesses. To complete the fabrication of the photodiode, 15 nm MoO₃, followed by 100 nm Ag, was deposited on top of the BHJ film through thermal evaporation in a vacuum chamber with a pressure of 3×10^{-6} mbar. The effective areas of the photodetectors were 9 mm². The devices were encapsulated between a cover glass bonded with epoxy.

Characterization: The current–voltage characteristics were measured with a Keithley 2400 Sourcemeter. Laser diodes with either 980 or 1310 nm emission wavelength was used as light sources. A series of neutral density filters were used to adjust the illumination power. In the EQE measurements using a monochromatic light source chopped at 400 Hz, the photocurrents were amplified through a low-noise amplifier and measured with a lock-in amplifier. Cutoff filters at 455, 645, and 1025 nm were used to reduce the scattered light from higher order diffraction. The lock-in amplifier allows accurate photocurrent measurement down to 2×10^{-10} A.

For the transient photoconductivity measurements, a pulsed laser with <10 ns pulse width and an emission wavelength of 520 nm was used as the light source. The intensity of the pulsed laser was adjusted to 20 mW cm⁻² so that photogenerated charge density was below 20% of the CV_{eff} (where C is the device capacitance and V_{eff} is the effective voltage) and space-charge effects were avoided. A 1.5 V battery connected in series to a potentiometer adjustable to 100 Ω was used to apply external bias on the photodiode. The photodiode was in series with the load resistor of 50 Ω , and the photocurrent was measured with an oscilloscope as the voltage dropped across the load resistor. Each curve in Figure 3 is an average of 64 measurements on the oscilloscope and 5 trials for each applied voltage. The BHJ thickness of the CPDT-TQ:PC₇₁BM device was 135 nm, and the P3HT:PC₇₁BM was 160 nm.

The noise spectral densities of the photodiodes were obtained by amplifying the dark current through a preamplifier (SRS 570) connected to a power spectrum analyzer (HP 89410A). The impedance spectroscopy of the photodiodes was measured by a potentiostat (Bio-Logic SP200).

In the spectroscopic analysis, monochromatic light with intensity between 5 and 10 μW was passed through the liquid mixtures in cuvettes and subsequently detected by an organic SWIR photodiode. The background signal of an empty cuvette was subtracted from transmission spectra of the liquid mixtures.

Supporting Information

Supporting Information is available from the Wiley Online Library or from the author.

Acknowledgements

The authors Z.W., W.Y., and T.N.N. are grateful for the support from American Chemical Society Petroleum Research Funds 57204-ND7. J.D.A. and A.E.L. are grateful for support from the National Science Foundation (NSF OIA-1632825 and DGE-1449999).

Conflict of Interest

The authors declare no conflict of interest.

Keywords

bulk heterojunctions, electric-field dependence, infrared photodiodes, organic semiconductors, thermal noise

Received: January 16, 2018
Revised: February 10, 2018
Published online: March 9, 2018

-
- [1] A. Rogalski, *Infrared Phys. Technol.* **2011**, *54*, 136.
[2] R. Saran, R. J. Curry, *Nat. Photonics* **2016**, *10*, 81.
[3] V. Adinolfi, E. H. Sargent, *Nature* **2017**, *542*, 324.
[4] J. W. Lee, D. Y. Kim, S. Baek, H. Yu, F. So, *Small* **2016**, *12*, 1328.
[5] F. H. L. Koppens, T. Mueller, P. Avouris, A. C. Ferrari, M. S. Vitiello, M. Polini, *Nat. Nanotechnol.* **2014**, *9*, 780.
[6] X. Gong, M. Tong, Y. Xia, W. Cai, J. S. Moon, Y. Cao, G. Yu, C.-L. Shieh, B. Nilsson, A. J. Heeger, *Science* **2009**, *325*, 1665.
[7] J. D. Zimmerman, V. V. Diev, K. Hanson, R. R. Lunt, E. K. Yu, M. E. Thompson, S. R. Forrest, *Adv. Mater.* **2010**, *22*, 2780.
[8] M. Young, J. Suddard-Bangsund, T. J. Patrick, N. Pajares, C. J. Traverse, M. C. Barr, S. Y. Lunt, R. R. Lunt, *Adv. Opt. Mater.* **2016**, *4*, 1027.
[9] A. London, L. Huang, B. Zhang, B. Oviedo, J. Tropp, W. Yao, Z. Wu, B. Wong, T. N. Ng, J. D. Azoulay, *Polym. Chem.* **2017**, *8*, 2922.
[10] B. Siegmund, A. Mischok, J. Benduhn, O. Zeika, S. Ullbrich, F. Nehm, M. Bohm, D. Spoltore, H. Frob, C. Korner, K. Leo, K. Vandewal, *Nat. Commun.* **2017**, *8*, 15421.
[11] R. D. Jansen-van Vuuren, A. Armin, A. K. Pandey, P. L. Burn, P. Meredith, *Adv. Mater.* **2016**, *28*, 4766.
[12] J. Benduhn, K. Tvingstedt, F. Piersimoni, S. Ullbrich, Y. Fan, M. Tropiano, K. A. McGarry, O. Zeika, M. K. Riede, C. J. Douglas, S. Barlow, S. R. Marder, D. Neher, D. Spoltore, K. Vandewal, *Nat. Energy* **2017**, *2*, 17053.
[13] L. Dou, Y. Liu, Z. Hong, G. Li, Y. Yang, *Chem. Rev.* **2015**, *115*, 12633.
[14] K. J. Baeg, M. Binda, D. Natali, M. Caironi, Y. Y. Noh, *Adv. Mater.* **2013**, *25*, 4267.
[15] C. L. Braun, *J. Chem. Phys.* **1984**, *80*, 4157.
[16] V. D. Mihailetschi, L. J. A. Koster, J. C. Hummelen, P. W. M. Blom, *Phys. Rev. Lett.* **2004**, *93*, 19.
[17] P. W. M. Blom, V. D. Mihailetschi, L. J. A. Koster, D. E. Markov, *Adv. Mater.* **2007**, *19*, 1551.
[18] R. A. Street, *Adv. Mater.* **2016**, *28*, 3814.
[19] Y. Fang, J. Huang, *Adv. Mater.* **2015**, *27*, 2804.
[20] Y. Zhou, C. Fuentes-hernandez, J. Shim, J. Meyer, A. J. Giordano, H. Li, P. Winget, T. Papadopoulos, H. Cheun, J. Kim, M. Fenoll, A. Dindar, W. Haske, E. Najafabadi, T. M. Khan, H. Sojoudi, S. Barlow, S. Graham, J. Brédas, S. R. Marder, A. Kahn, B. Kippelen, *Science* **2012**, *873*, 327.
[21] N. Zhou, M. Kim, S. Loser, J. Smith, H. Yoshida, X. Guo, C. Song, H. Jin, Z. Chen, S. M. Yoon, A. Freeman, R. P. H. Chang, A. Facchetti, T. J. Marks, *Proc. Natl. Acad. Sci. USA* **2015**, *112*, 7897.
[22] P. Schulz, S. R. Cowan, Z. L. Guan, A. Garcia, D. C. Olson, A. Kahn, *Adv. Funct. Mater.* **2014**, *24*, 701.
[23] R. A. Street, M. Schoendorf, A. Roy, J. H. Lee, *Phys. Rev. B* **2010**, *81*, 205307.
[24] T. N. Ng, W. S. Wong, R. A. Lujan, R. A. Street, *Adv. Mater.* **2009**, *21*, 1855.
[25] C. G. Shuttle, R. Hamilton, B. C. O'Regan, J. Nelson, J. R. Durrant, *Proc. Natl. Acad. Sci. USA* **2010**, *107*, 16448.
[26] J. Kniepert, M. Schubert, J. C. Blakesley, D. Neher, *J. Phys. Chem. Lett.* **2011**, *2*, 700.
[27] R. A. Marsh, J. M. Hodgkiss, R. H. Friend, *Adv. Mater.* **2010**, *22*, 3672.
[28] J. D. Servaites, M. A. Ratner, T. J. Marks, *Energy Environ. Sci.* **2011**, *4*, 4410.
[29] T. M. Clarke, J. R. Durrant, *Chem. Rev.* **2010**, *110*, 6736.
[30] M. Lenes, L. J. A. Koster, V. D. Mihailetschi, P. W. M. Blom, *Appl. Phys. Lett.* **2006**, *88*, 86.
[31] S. Gélinas, O. Paré-Labrosse, C. N. Brosseau, S. Albert-Seifried, C. R. McNeill, K. R. Kirov, I. A. Howard, R. Leonelli, R. H. Friend, C. Silva, *J. Phys. Chem. C* **2011**, *115*, 7114.
[32] N. D. Eisenmenger, K. T. Delaney, V. Ganesan, G. H. Fredrickson, M. L. Chabiny, *J. Phys. Chem. C* **2015**, *119*, 19011.
[33] M. Stolterfoht, A. Armin, S. Shoaee, I. Kassal, P. Burn, P. Meredith, *Nat. Commun.* **2016**, *7*, 11944.
[34] K. Vandewal, S. Albrecht, E. T. Hoke, K. R. Graham, J. Widmer, J. Douglas, M. Schubert, W. R. Mateker, J. T. Bloking, G. Burkhard, A. Sellinger, J. M. Frechet, A. Amassian, M. K. Riede, M. McGehee, D. Neher, A. Salleo, *Nat. Mater.* **2014**, *13*, 63.
[35] R. A. Street, S. Cowan, A. J. Heeger, *Phys. Rev. B: Condens. Matter Mater. Phys.* **2010**, *82*, 11.
[36] F. Fabregat-Santiago, G. Garcia-Belmonte, I. Mora-Seró, J. Bisquert, *Phys. Chem. Chem. Phys.* **2011**, *13*, 9083.
[37] G. Grancini, M. Maiuri, D. Fazzi, A. Petrozza, H.-J. Egelhaaf, D. Brida, G. Cerullo, G. Lanzani, *Nat. Mater.* **2012**, *12*, 29.
[38] B. G. F. Burkhard, E. T. Hoke, M. D. McGehee, *Adv. Mater.* **2010**, *22*, 3293.
[39] H. Liu, Z. Wu, J. Hu, Q. Song, B. Wu, H. Lam Tam, Q. Yang, W. H. Choi, F. Zhu, *Appl. Phys. Lett.* **2013**, *103*, 43309.
[40] Z. Wu, B. Wu, H. Tam, F. Zhu, *Org. Electron.* **2016**, *31*, 266.
[41] R. A. Street, Y. Yang, B. C. Thompson, I. McCulloch, *J. Phys. Chem. C* **2016**, *120*, 22169.
[42] Z. Tang, Z. Ma, A. Sánchez-Díaz, S. Ullbrich, Y. Liu, B. Siegmund, A. Mischok, K. Leo, M. Campoy-Quiles, W. Li, K. Vandewal, *Adv. Mater.* **2017**, *29*, 1702184.
[43] D. B. Sulas, A. E. London, L. Huang, L. Xu, Z. Wu, T. N. Ng, B. M. Wong, C. W. Schlenker, J. D. Azoulay, M. Y. Sfeir, *Adv. Opt. Mater.* **2018**, <https://doi.org/10.1002/adom.201701138>.
[44] T. Rauch, M. Boberl, S. F. Tedde, J. Furst, M. Kovalenko, G. Hesser, U. Lemmer, W. Heiss, O. Hayden, *Nat. Photonics* **2009**, *3*, 332.
[45] Z. Wu, W. Yao, A. E. London, J. D. Azoulay, T. N. Ng, *ACS Appl. Mater. Interfaces* **2017**, *9*, 1654.
[46] C. M. Lochner, Y. Khan, A. Pierre, A. C. Arias, *Nat. Commun.* **2014**, *5*, 1.
[47] T. Yokota, P. Zalar, M. Kaltenbrunner, H. Jinno, N. Matsuhisa, H. Kitanosako, Y. Tachibana, W. Yukita, M. Koizumi, T. Someya, *Sci. Adv.* **2016**, *2*, e1501856.
[48] E. Thimsen, B. Sadtler, M. Y. Berezin, *Nanophotonics* **2017**, *6*, 1043.
[49] T. N. Ng, D. E. Schwartz, P. Mei, B. Krusor, S. Kor, J. Veres, P. Bröms, T. Eriksson, Y. Wang, O. Hagel, C. Karlsson, *Sci. Rep.* **2015**, *5*, 13457.
[50] Hermann-Jens Womelsdorf, *US6710091B1*, **2000**, 8.